Charged Fibrous Viruses (fd) in External Electric Fields: Dynamics and orientational order

Kyongok Kang

Forschungszentrum Jülich, IFF-7, Weiche Materie (Soft Matter)
D-52425 Jülich
Germany

Abstract

We recently found a number of phases and dynamical states that are induced in a concentrated suspension of charged, colloidal rods (fd-viruses) by an alternating external electric field [Euro. Phys. Lett. **84**, 14005 (2008); Soft Matter, **6**, 273 (2010)]. The various phases and dynamical states are the result of interactions between the charged rods through their polarized electric double layers, polarized layers of condensed ions and/or electro-osmotic flow. At relatively high frequency, a homogenous, homeotropically aligned phase is induced (the H-phase). We present a dynamic light scattering study of the microscopic dynamics of the rods, varying the frequency and field amplitudes along different pathways within this phase. Scattering experiments are performed at very small scattering angles with a home-made vertically mounted dynamic light scattering set up, where Brownian motion perpendicular to the direction of alignment is probed. The orientational order is measured by means of birefringence experiments. The remarkable finding is that relaxation times and the degree of alignment are independent of the frequency and the amplitude of the applied electric field throughout the entire H-phase. Only within a small region in the neighborhood of the transition line where the H-phase transforms to an inhomogeneous chiral-nematic phase, there is a frequency and amplitude dependence of relaxation times, which are shown to be the result of the appearance of transient, pre-transitional domains. We also recently identified a non-equilibrium critical point, where a time- and length-scale connected to a dynamical state are shown to diverge [Eur. Phys. J. E, **30**, 333 (2009)]. Approaching this critical point from the side of the H-phase, we find that the light scattering correlation functions develop a very slowly decaying mode, the origin of which requires further investigation.

1 Introduction

Dynamical properties of charged colloidal rods in an external electric field are generally affected by interactions between the rods through the field-induced polarization of their double layer and/or their core. At high frequencies (in the MHz range) and relatively high field amplitudes, the cores

of the colloids are dielectrically polarized giving rise to dipolar interactions between the colloids, which can lead to structure formation such as strings and sheets [1],[2],[3]. At such high frequencies, electric-double layers around the charged rods (fd-virus particle with a length of $L = 880\ nm$, a bare diameter of $D = 6.6\ nm$, a persistence length at high salt concentration of $P = 2200\ nm$) are not polarized due to the finite mobility of the ions that constitute the double layer. Double layer-polarization is important only for relatively low frequencies. Besides interactions between rods through their polarized double layers, there are two additional field-induced forces that may play a role, which are related to condensed ions and electro-osmotic flow. The origin of the field-induced forces at low frequencies is sketched in Fig.1. In the absence of an external field, the electric double layer is cylindrically symmetric, as sketched in Fig.1a. On applying an electric field, the double layer of a rod becomes asymmetric, the layer of condensed ions is polarized, and electro-osmotic flow is induced due to electrical body forces on charged volume elements within the double layer, as sketched in Fig.1b. In concentrated suspensions, rods interact with each other due to the polarized double layer, the polarized layer of condensed ions, and hydrodynamically through electro-osmotic flow, as sketched in Fig.1c. So far, very little research has been done on phase transitions that can be induced at low frequencies as a result of these field-induced interactions. As far as we know, no research has so far been done on the microscopic dynamics of charged rods in phases that are induced by low-frequency electric fields, which might shed light on the relative importance of the three above mentioned types of interactions.

We recently found that various phases and dynamical states can be induced in suspensions of charged colloidal rods (fd-viruses), where the concentration of fd-viruses is such that there is an isotropic-nematic coexistence in the absence of the field [4],[5]. One of the induced phases, which is of interest in the present paper, is a homogeneous phase with homeotropic alignment of the rods. We referred to this phase as the H-phase. This phase is found for frequencies larger than about a kHz, where there is only a weak polarization of the double layer [6], so that the two other forces discussed above might be dominant. Interactions due to electro-osmotic flow has been investigated by simulations in Ref.[7] for two rods with thin double layers. Interactions through the polarization of the

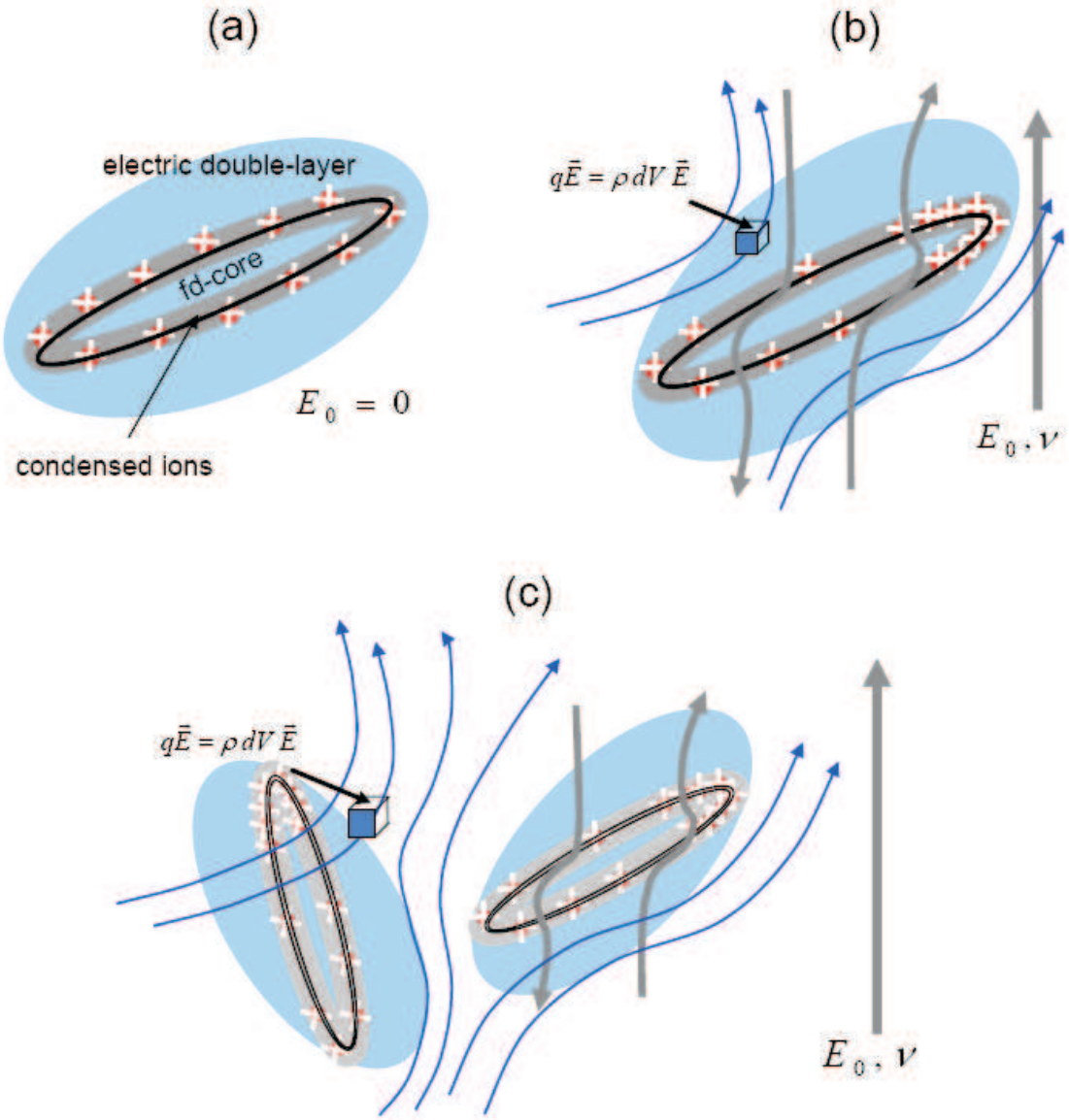

Figure 1: (a) A charged rod in the absence of an external field, with a cylindrical symmetric double layer and a symmetric layer of condensed ions. (b) In a low-frequency electric field the double layer is polarized, the layer of condensed ions is polarized, and electro-osmotic flow is induced. A small charged volume element is shown on which an electric body force acts that leads to electro-osmotic flow. (c) Two rods which interact through their polarized double layer and layer of condensed ions, as well as hydrodynamically through the induced electro-osmotic flow.

layers of condensed ions have very recently been analyzed, for zero frequency, by Manning [8],[9]. This analysis suggests that the change in preferred orientation found for fd-suspensions in Refs.[10],[11] is due to polarization of the layer of condensed ions (although the experiments have been performed with alternating fields). It is not yet clear which of the possible interactions are responsible for the stabilization of the H-phase. *It is the purpose of the present paper to characterize the fd-virus dynamics and orientational order in the H-phase, in order to sustain possible future theoretical predictions on the interactions between charged colloidal rods in low-frequency external fields.*

This paper is organized as follows. We start with a section on the experimental details. In subsection 2.1, the characteristics of fd-virus particles and their suspensions are presented. Subsection 2.2 introduces the electrical cell and the dynamic light scattering set up. Subsection 2.3 is a resume of the phase/state-behavior of a fd-virus suspensions in an electric field with varying field amplitude and frequency. The orientational order, along different pathways within the H-phase, is discussed in section 3. The pathways include regions in the phase/state diagram that are in the vicinity of transition lines. In section 4 the microscopic dynamics, as probed with dynamic light scattering, along the same pathways is discussed. Finally conclusions are in section 5.

2 Experimental Details

In this section the properties of fd-virus particle suspensions and their preparation are discussed, we describe the technical details of the electrical sample cell and the small angle dynamic light scattering set up, and summarize the phases and dynamical states that can be induced in fd suspensions by means of an electric field.

2.1 Charged fibrous virus (fd) suspensions

Bacteriophage fd is a rod-like macromolecule with a length of $L = 880\ nm$, a bare diameter of $D = 6.6\ nm$, a persistence length at high salt concentration of $P = 2200\ nm$, and a molecular weight of $M = 1.64 * 10^7\ g/mol$. The hydrodynamic properties (and structure) of fd-virus particles are discussed in Ref.[12].

The fd-viruses are grown and purified following standard biological protocols [13] using the XL1blue

strain of E. coli as the host bacteria. The virus particles are purified by repeated centrifugation ($10^5\,g$ for 5 hours) and re-dispersed in TRIS/HCl buffers with varying concentration, depending on the desired final ionic strength. From the dimensions and molecular weight of an fd-virus particle, the volume fraction φ of an fd-virus suspension is found to be related to the weight concentration c, as $\varphi = 1.10{*}10^{-3}\ c\ [\,mg/ml\,]$. The overlap concentration of fd-virus suspensions is equal to 0.076 mg/ml.

We prepare fd-virus suspensions at a given ionic strength by osmotic equilibration with a TRIS/HCl buffer. The same buffer is used to dilute the suspensions (by typically 20 %) to the desired fd concentration. The ionic strength of the osmotic reservoirs is the ionic strength from which the electrostatic Debye-Hückel screening length is calculated. Furthermore, osmotic equilibration assures that the pH of the suspensions is equal to those of the osmotic reservoir. The TRIS/HCl buffers are prepared by adding a small volume of HCl with a concentration of 1 M to a 20.0 mM TRIS solution till a pH of 8.2 is attained. This buffer is then diluted with deionized water for the preparation of the lower TRIS/HCl-buffer concentrations. For buffer concentrations less than about 10 mM, both the ionic strength and the pH are affected by carbon dioxide that dissolves from the air, which in turn affects the surface charges of the fd-virus particles. A detailed account of the effect of dissolved carbon dioxide on the ionic strength and pH as a function of the buffer concentration can be found in Ref.[14].

The charge distribution on fd-virus particles has been interpreted on the basis of different models for an fd-virus particle from titration curves. The best fit to titration curves is found when assuming that the charges are located only on the hydrophilic outer region of adsorbed coat proteins, and not on the DNA strand of fd itself [15]. The iso-electric point of native fd is equal to $pH = 4$. In the present study we use the pH is always larger than 6.5, where the fd particles are negatively charged. The charge of an fd-virus particle varies in the range $-10000 \leq Q_{fd} \leq -8500$ in the pH-range $6.5 \leq pH \leq 8.2$ [15]. The buffer capacity of the low-ionic strength TRIS/HCl buffer that we used is still sufficient to keep the pH above 6.5, despite dissolving carbon dioxide from the air [14].

In a previous study on the response of fd-virus suspensions to electric fields, it was found that no phase transition could be induced for concentrations outside isotropic-nematic coexistence region [5]. The fd-concentrations are therefore chosen within the bi-phasic isotropic-nematic coexistence

region, in the absence of an electric field. The buffer concentration is 0.16 mM. The Debye-screening length for water at 25^0C, using that $\kappa_Q^{-1}\,[nm] = 0.304/\sqrt{I\,[M]}$ (with I the ionic strength corrected for dissolving carbon dioxide [14]) is found to be equal to $27\,nm = 4.1\,D$.

2.2 The electrical cell and small angle vertical dynamic light scattering set up

A home-made optically transparent electrical cell is used to facilitate dynamic light scattering, imaging through a microscope and birefringence measurements. The sample is contained between two horizontal parallel ITO glass plates, with a spacer of $1.4\,mm$ thickness. The conductive ITO coatings are connected to a function generator. The dynamical light scattering set up is vertically mounted, where the direction of incidence of a $5\,mWatt$ He-Ne laser is along the electric field, vertical to the two plates. Scattered light is collected through a fiber that is connected to an avalanche photo diode detector. The set up is used in VV mode. The VH-scattered intensities from fd-virus suspensions are too low to measure reliable correlation functions.

Due to refraction of scattered light from the sample-glass and glass-air interfaces, the true scattering angle Θ_s is not equal to the goniometer angle Θ_g (see Fig.2a). The ratio of the true scattering wave vector q and the apparent scattering wave vector q_g as calculated from the goniometer angle is given in Fig.2b as a function of the goniometer angle. As can be seen from this plot, the scattering wave vector is significantly affected by interface refraction only for scattering angles larger than about 20^0.

At small scattering angles, the scattering vector is essentially perpendicular to the direction of the external electric field, as sketched in Fig.2c. For larger scattering angles, there is a small contribution to the scattering wave vector that is parallel to the external field. The relative values of the perpendicular $q_\perp$ and parallel $q_\parallel$ components to the total scattering wave vector are plotted in Fig.2d. As can be seen, up to about 15^0 scattering angle, only the dynamics related to motion perpendicular to the electric field is probed, while for larger scattering angles also a small contribution from motion parallel to the electric field is involved.

An essential part of the vertical dynamical light scattering set up involves a lens (with focal length

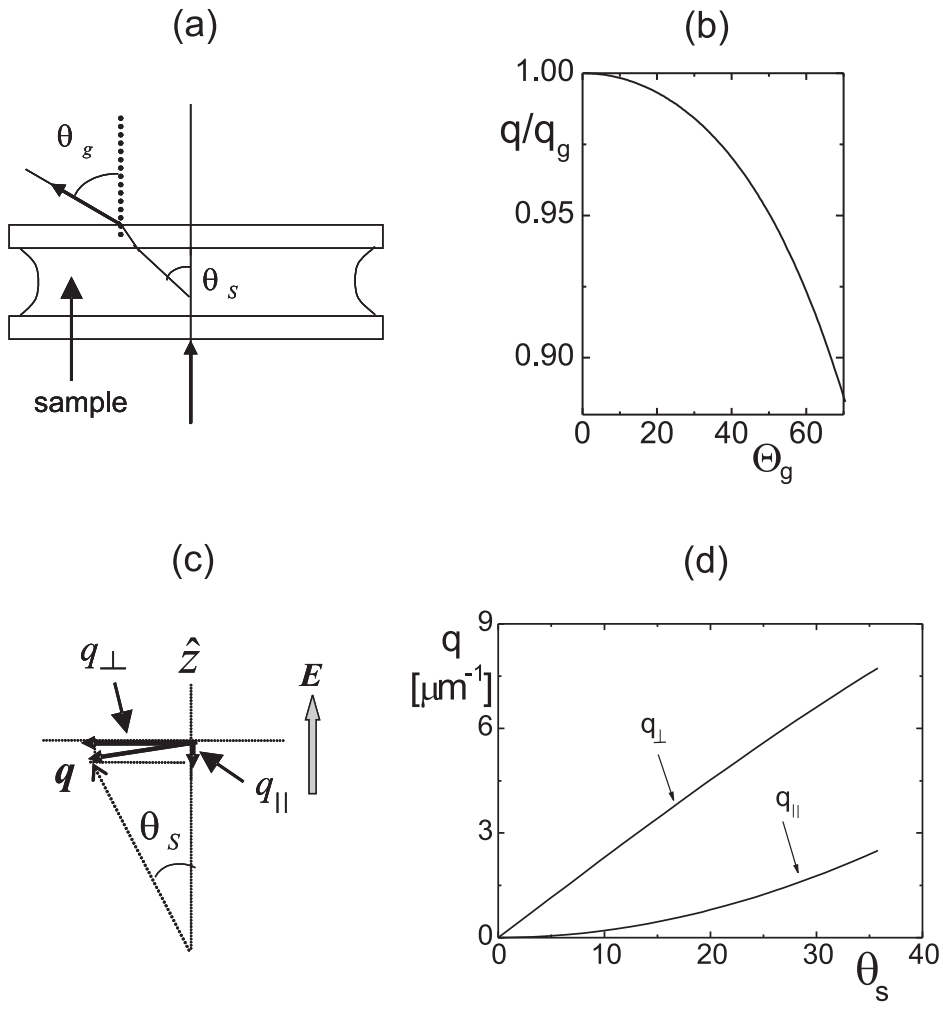

Figure 2: (a) Due to refraction, the true scattering angle Θ_s differs from the goniometer angle Θ_g in degrees. (b) The ratio of the true scattering vector q and the scattering vector q_g as calculated from the goniometer angle as a function of the goniometer angle. (c) The scattering geometry of the vertical small angle dynamic light scattering set up. The electric field **E** and the laser beam are both along the z-direction. The main component of the scattering vector is perpendicular to the electric field ($q_\perp$), while for larger scattering angles there is also a small but significant parallel component ($q_\parallel$). (d) The perpendicular and parallel components of the scattering vector as a function of the scattering angle in degrees.

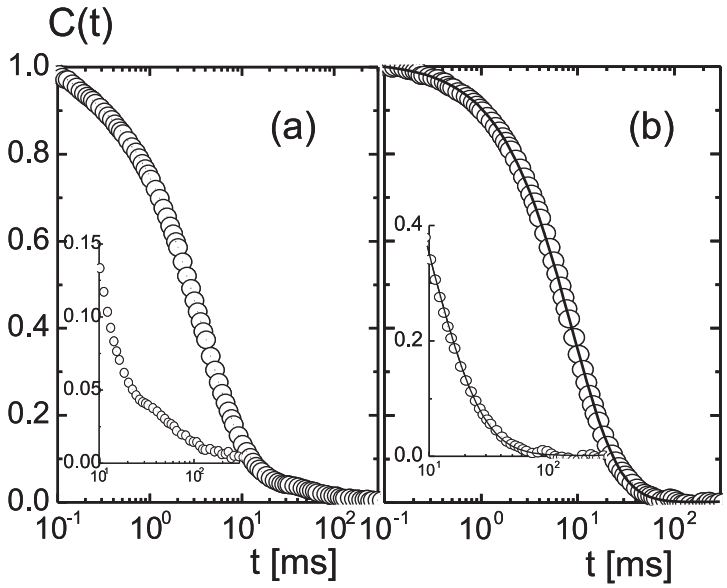

Figure 3: Normalized correlation function of a dilute suspension of silica particles (diameter 166 nm) at a scattering angle of 9.6^0: (a)without the 75 mm focal-length lens, and (b) with the lens. The insets show the correlation functions at longer times. The solid line in (b) is a fit to a single exponential decay.

75 mm) that ensures that only light that is scattered from the bulk part of the sample is probed. Figs.3a,b show the normalized intensity correlation functions for a dilute silica-sphere suspension as measured without and with this lens, respectively. As can be seen, the long-time behavior of the correlation functions (also shown in the insets) is quite different. Without the lens, scattering by particles near the wall leads to spurious slow relaxation. The dynamics of particles near the wall is severely slowed down by hydrodynamic interactions with the wall. The single-exponential behavior of the correlation function that is expected for dilute suspensions of spheres in bulk is indeed found for the set up with the lens. This can be seen from the solid line in Fig.3b, which is a fit to a single exponential decay.

2.3 Electric Phase/state Diagrams of fd-suspensions

In two earlier publications [4],[5] a number of driven phases and dynamical states in fd-virus suspensions were found, which are induced by means of an external electric field. The frequencies are small enough to polarize the electrical double layers of the fd-virus particles. The new phases and states are the result of interactions between fd-virus particles through their polarized double, due to polar-

ization of the layer of condensed ions and/or electro-osmotic flow. The phase/state diagram for an fd concentration of $2.0\,mg/ml$ and a TRIS/HCL-buffer concentration of $0.16\,mM$ in the field-amplitude verses frequency plane are given in Fig.4. The concentration is within the isotropic-nematic biphasic region in the absence of an electric field. Detailed characterizations of the various transition lines are published in Ref.[5]. The following phases and dynamical states are found: The N-phase in the phase diagram in Fig.4 refers to a coexistence between nematic domains and isotropic regions. A typical depolarized-microscopy image is given below the phase/state diagram in Fig.4. On increasing the field amplitude at low frequencies, the inter-rod interactions mentioned above give rise to a transition to the $N^\star$-phase, which is a coexistence between nematic domains and chiral-nematic domains. The chiral-nematic regions extend over much larger regions as compared to the non-chiral nematic domains. Two images for the $N^\star$-phase are shown in Fig.4, one at low frequency (on the left side) and one at high frequency (on the right side). As can be seen, the pitch is markedly larger at high frequencies, near the H-to-$N^\star$ transition line, as compared to the pitch at low frequency. On further increasing the field amplitude, the N-domains disconnect from each other and become significantly smaller within a small field-amplitude range, which we refer as the N_D^*-phase, where the subscript "D" stands for "disconnected". The difference between the typical morphologies of the $N^\star$- and $N_D^\star$-phases is shown in the left two images in Fig.4. The chiral texture melts at a certain higher field amplitude, and at the same time the N-domains melt and reform. This dynamical state is referred to as the D_s-state, a snap shot of which is given in the top of Fig.4. The subscript "s" stands for "slow". On increasing the field amplitude further, the dynamics of melting and formation becomes faster, referred to as the D_f-state, where the subscript "f" stands for "fast".

Of particular interest in the present study is the uniform phase at relatively high frequencies, where the fd-virus particles are homeotropically aligned, parallel to the external field. This homogeneous phase is referred to as the H-phase (where "H" stands for "homeotropic"). The corresponding morphology is given in the image on the right side in Fig.4. In the present paper we study the microscopic dynamics and the degree of alignment of the fd-rods in this H-phase, varying both the frequency and field amplitude.

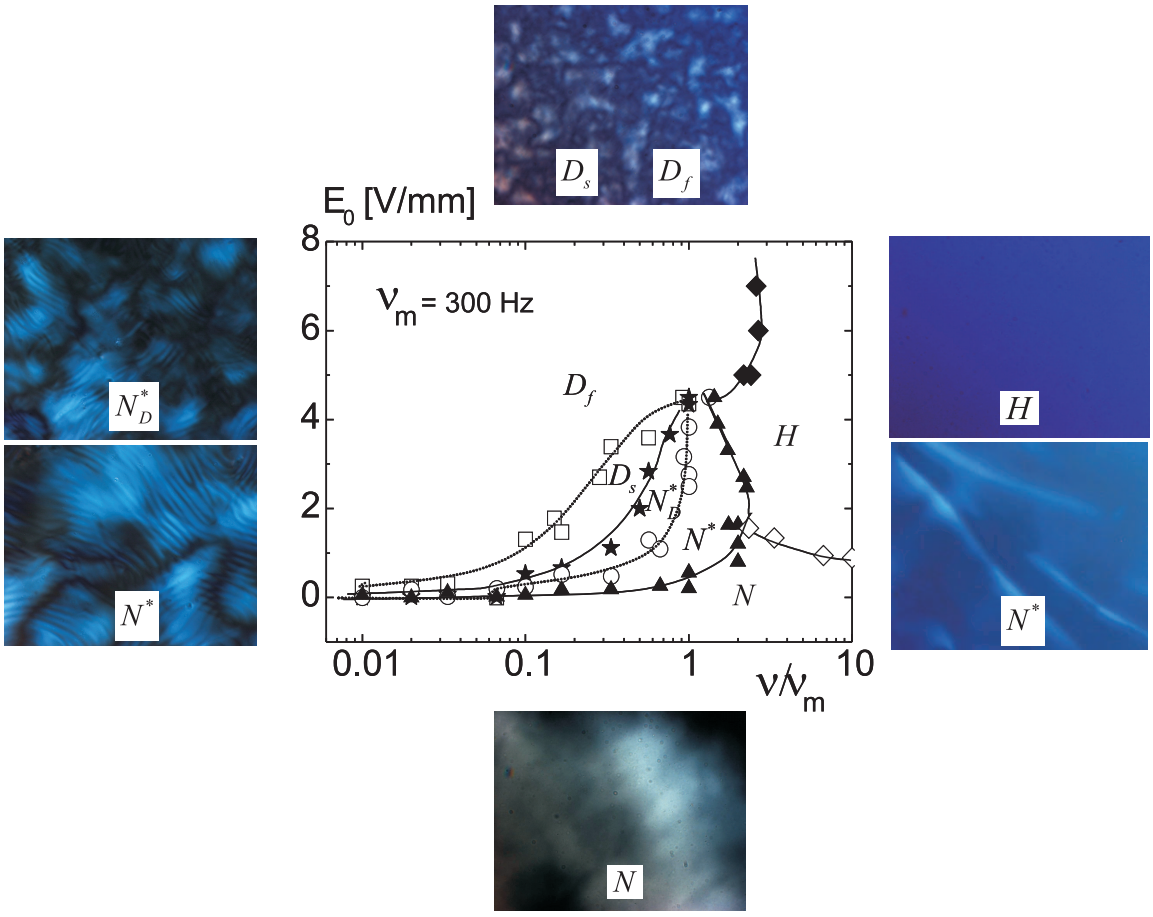

Figure 4: Electric phase/state diagram of fd-virus suspensions in the field-amplitude versus normalized frequency plane for a fd concentration of 2.0 mg/ml. The buffer concentration is 0.16 mM. The solid lines refer to sharp phase/state transitions, while the dotted lines refer to more gradual transitions involving the chiral texture and dynamics of N-domains. The images show typical morphologies of the different phases/states, as obtained by polarization microscopy. Two morphologies are shown for the $N^\star$-phase, one at low frequency and one at high frequency, showing the increase of the pitch with increasing frequency. The field of view in these images is $430 \times 320\ \mu m^2$. Note that the frequency is normalized by the frequency $\nu_m = 300\, Hz$ where the critical point occurs.

The solid lines in the phase/state diagrams in Fig.4 refer to sharp phase/state-transition lines, whereas the dotted lines refer to gradual transitions (the $N^\star$-to-$N_D^\star$ and D_s-to-D_f transitions).

There is a special point, where in the phase/state diagram in Fig.4 various phase/state-transition lines meet. It resembles a critical point in equilibrium phase diagrams. On approach of this point from the side of the dynamical state, like for equilibrium critical points, a divergent length- and time-scale can be identified. As shown in ref.[16], the size of the melting and forming nematic domains in the dynamical state, and the time scale on which melting/forming evolves, both diverge on approach of this non-equilibrium critical point. As will be seen in the present study, there are also signatures for critical behavior on approach of the critical point from the side of the H-phase.

3 Electric Birefringence

Electric birefringence measurements are performed for a fd concentration of 2.0 mg/ml along various path ways within the H-phase, where either the field amplitude is varied at fixed frequency, or the frequency is varied at a fixed field amplitude. in the electric phase/state diagram. The following pathways have been probed:

- Pathway (i): varying field amplitude at a fixed frequency of $\nu = 2\,kHz$.
- Pathway (ii): varying frequency at a fixed field amplitude of $E = 2.9\,V/mm$.
- Pathway (iii): varying frequency at a fixed field amplitude of $E = 3.5\,V/mm$.

The field amplitude for pathway (iii) is the critical field amplitude, that is, the field amplitude where the non-equilibrium point in the phase/state diagram in Fig.4 is located [16]. On lowering the frequency along pathway (iii), the critical point is thus approached. Note that the critical field amplitude in the phase diagram Fig.4 is a bit higher than $3.5\,V/mm$. As discussed in Ref.[5], this is related to the finite measuring time for the data points in the phase diagram in combination with critical slowing down of dynamics near the critical point. Accurate values for the critical amplitude and frequency have been determined in Ref.[16]. On lowering the frequency along pathway (ii), the off-critical part of the H-to-$N^\star$ transition line is approached. The H-to-N transition line is approached along pathway (i) on lowering the field amplitude.

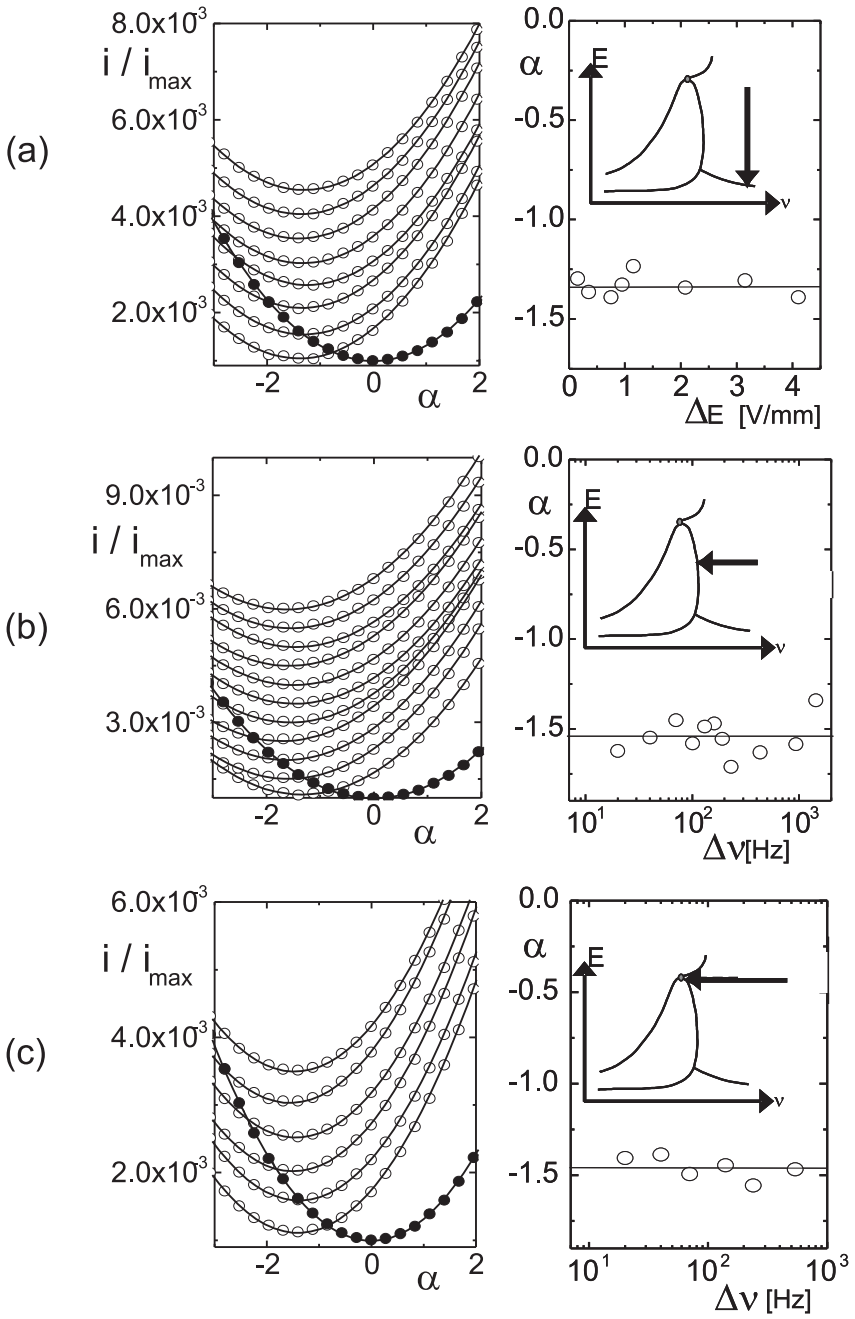

Figure 5: Birefringence measurements for the pathway (i) (upper two plots, (a)), pathway (ii) (middle two plots, (b)), and pathway(iii)(lower two plots, (c)). The left plots are measured transmitted intensities as a function of the analyzer angle α in degrees, and the right set of figures are the phase shifts as a function of field amplitude ΔE or frequency $\Delta\nu$ relative to the transition values. Here the horizontal lines indicate the average value of the obtained analyzer angle shift α in degrees. The filled circles in the plots on the left correspond to pure buffer. Subsequent curves are vertically shifted by 0.0005 for clarity. (a) From below to top: $\Delta E = 1.00$, 1.20, 1.60, 1.80, 2.00, 2.93, 4.00 and $4.95\,V/mm$. (B) From below to top: $\Delta\nu = 20$, 40, 70, 100, 130, 160, 190, 230, 430, 930, $1430\,Hz$. (C) From below to top: $\Delta\nu = 10$, 30, 60, 130, 230, $530\,Hz$.

The $He-Ne$ laser beam of the vertically mounted, null-optical-train birefringence set up makes an angle of 20^o with the direction of the external electric field. Since in the H-phase the rods are aligned along the external field, no birefringence would be detected in case of a normal incidence onto the sample cell. A description of the experimental set up and a detailed analysis on the interpretation of such birefringence measurements is given in Ref.[5]. In a null-optical-train birefringence set up, the transmitted intensity is measured as a function of the orientation of a polarizer. The analyzer angle where the minimum transmitted intensity is found, relative to that of pure buffer, is equal to half the birefringence retardation. The retardation is in turn proportional to the orientational order parameter, where the proportionality constant depends on the angle of incidence of the laser beam [5].

The left column of plots in Fig.5a,b,c gives birefringence data for the three pathways (i), (ii) and (iii), as defined above, respectively. These plots are transmitted intensities (relative to the maximum transmitted intensity) as a function of the analyzer angle α in degrees. The filled circles are data for the pure buffer and the open circles are data for the fd suspension (curves are consecutively vertically shifted by 0.0005 for clarity). The right column in Fig.5 shows the analyzer angle where the minimum intensity is found, relative to the pure buffer, as a function of the distance from the transition lines; ΔE for pathway (i), and $\Delta\nu$ for pathways (ii) and (iii). As can be seen, the analyzer angle where the minimum transmitted intensity is surprisingly found to be equal to 1.4^0 (to within an experimental error of $0.3\,^0$), independent of the field amplitude and frequency. The corresponding value for the orientational order parameter is 0.38 ± 0.08, and is the same throughout the H-phase.

The independence of the degree of alignment on both the field amplitude and frequency could be explained as follows. The ions within the diffuse double layer (about 15% of the total charge) and the condensed ions (about 85%) have a finite diffusivity. At sufficiently high frequencies, therefore, the polarization of the double layer and the layer of condensed ions become less important. For frequencies above a few kHz range, the ions in the diffuse double layer and in the layer of condensed ions can not follow the external field anymore. The establishment of electro-osmotic flow, on the contrary, is very fast (on the ns time scale), so that electro-osmotic flow remains active also at high frequencies. Since

polarization would lead to a field-amplitude dependent response, we anticipate that electro-osmotic flow gives rise to the stability of the H-phase.

As shown in Ref.[5], a significantly aligned state can not be induced at lower concentrations in the isotropic state. This implies that the alignment in the H-phase is due to rod-rod interactions induced by the external field and not due to single-particle alignment.

Based on the above measurements of electric birefringence, we can conclude that the high frequency uniformly aligned homeotropic H-phase is governed by different interactions among fd-virus particles, which is not by the deformation of double layer, but by the electro-osmotic flow that acts on the small volume element in the solvent and double layers. This is quite substantially different for low frequency interactions, where mainly determined by the direct deformation of the double-layers in various phases/ states. Further investigations of the clear distinction between the possible mechanism of these frequency-response interactions are a follow up subject to study in both theory and experiments.

4 Diffusion perpendicular to the director: $\mathbf{q} \perp \mathbf{E}$

As discussed in subsection 2.2, for the very small scattering angles that can be accessed by our vertically mounted dynamic light scattering set up, diffusion perpendicular to the direction of alignment in the H-phase is probed. In this section we discuss the dynamics related to displacements perpendicular to the direction of alignment. Dynamic light scattering experiments at scattering angles less than 12^o along the same pathways (i), (ii) and (iii) as defined in the previous section on birefringence will be performed.

Dynamic light scattering measures the intensity auto-correlation function $C(t)$, the relaxation rate of which characterizes the dynamics of the rods. For the system under consideration of strongly interacting rods, the intensity auto-correlation function is generally a complicated function of time. Correlation function are commonly highly non-single exponential. The correlation functions obtained in our experiments are found to be described by a single, stretched exponential function,

$$C(t) \;=\; A \exp\left\{-2\left(\Gamma_\perp\, t\right)^\beta\right\} \;, \tag{1}$$

where A is the dynamical contrast, $\Gamma_\perp$ is the relaxation rate and β is the stretching coefficient. The need for a stretched exponential function is due to the many different relaxation modes that contribute due to the strong interactions between the fd-virus particles. Due to the finite size of the scattering volume, typical values for the dynamical contrast are around 0.5.

For larger frequencies, far away from transition lines, there is a very small amplitude contribution to the correlation functions of a fast relaxing mode, which is probably due to diffusion parallel to the director. The relative amplitude of this contribution is less than about 1 % at very small scattering angles, and is too small to affect the fitting values of the parameters in eq.(1). However, the amplitude of this fast mode is more pronounced at larger scattering angles. The contribution of the fast mode is more pronounced at higher fd concentrations and/or lower ionic strengths, which will be discussed in a separate paper.

Contrary to the off-critical path (ii), for which typical correlation functions are shown in Fig.6a, the correlation functions along pathway (iii) develop a very slow relaxing mode on approach of the critical point. This is shown in Fig.6b, where three correlation functions for various distances from the critical point are shown. The solid lines are fits to a stretched exponential in eq.(1), excluding the long times. Relaxation of the initial part is seen to become faster on approach of the critical point, due to pre-transitional domains as discussed above, while a very slow decaying tail develops with increasing amplitude and relaxation time near the critical point. This speeding up of the initial relaxation and slowing down of the long-time decay on approach of the critical point leads to a crossing of the two correlations for $\Delta\nu = 30$ and $100\,Hz$, as indicated by the circle in Fig.6b. In addition, the size of the pre-transitional domains is much larger as compared to the off-critical pathway. The identification of the point in the phase/state diagram where several transition lines meet as a critical point seems therefore not only meaningful on approach of that point from the dynamical state [16], but also from the side of the H-phase. The detailed features of the critical behavior on approach from the side of the H-phase requires further study and is outside the scope of the present study.

Relaxation rates along the pathways (i) and (ii) are given as a function of q^2 in Figs.7a,b. For pathway (i)in Fig.7a, the relaxation rate is seen to be independent of the field amplitude, right down

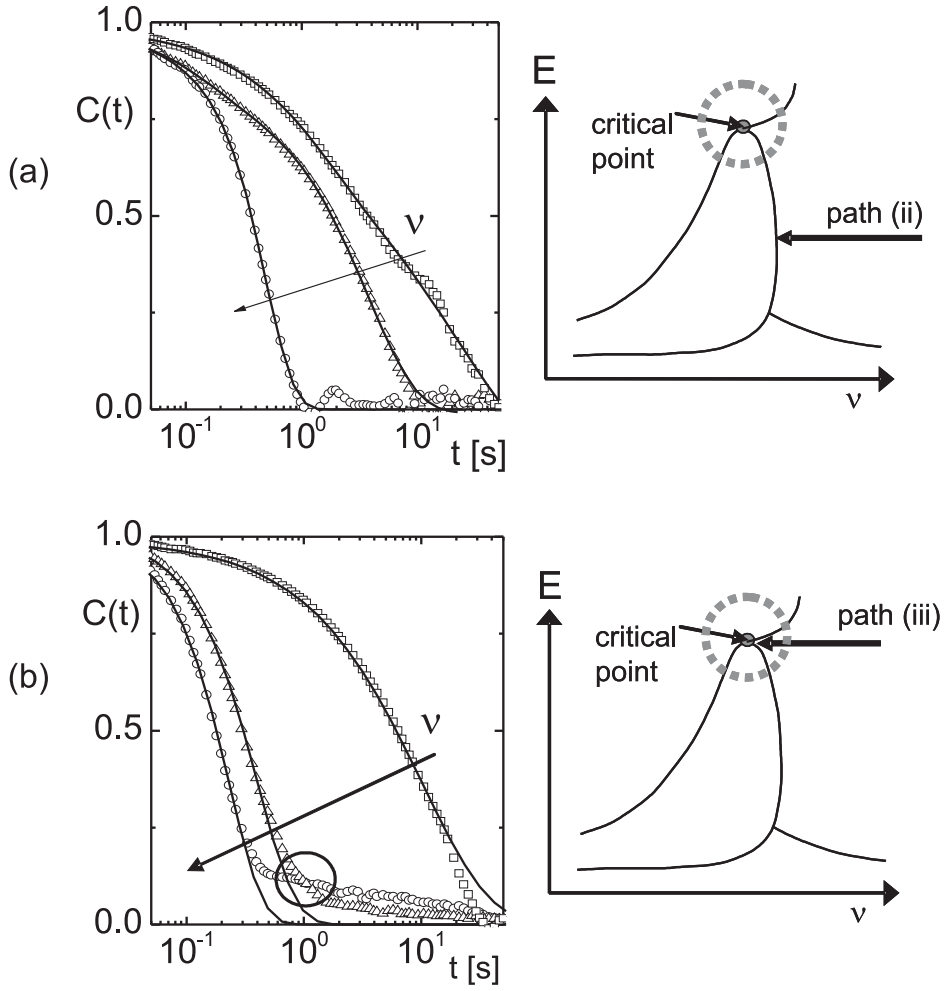

Figure 6: (a)Intensity auto-correlation functions along pathway (ii). The arrow indicates reducing frequency. All correlation functions are measured to within $200\,Hz$ from the H-to-$N^\star$ transition line. The measuring time was $30\,min$. (b)Intensity auto-correlation functions along pathway (iii) at the critical field amplitude $E = 3.5\,V/mm$ for three distances from the critical point: $\Delta\nu = 30$ (circles), 100 (triangles) and $2000\,Hz$ (squares). The measuring time for the two functions with the slow, critical mode is $10\,hours$. The solid lines are fits to a stretched exponential, excluding the long times. The circle indicates where the first two correlation function cross.

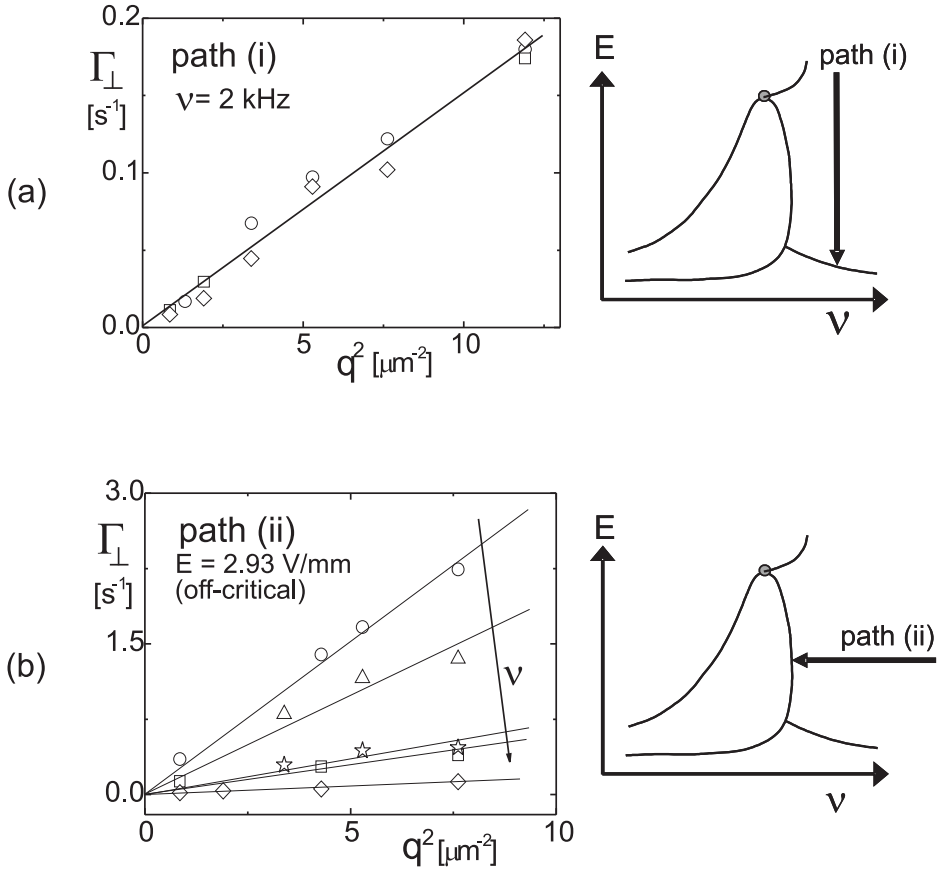

Figure 7: Relaxation rates versus the square of the wave vector (a) for pathway (i), and (b) for pathway (ii). These pathways are sketched in the top-right figures. In (a) for pathway (i): $\nu = 2\,kHz$, $\Delta E = 0.04 V/mm$ (circles), $0.30\,V/mm$ (squares) and $1.00\,V/mm$ (diamonds). In (b) for path (ii): $E = 2.93\,V/mm$, $\Delta\nu = 20\,Hz$ (circles), $40\,Hz$ (triangles), $90\,Hz$ (stars), $200\,Hz$ (squares), and $2000\,Hz$ (diamonds). Solid lines are guides-to-the-eye.

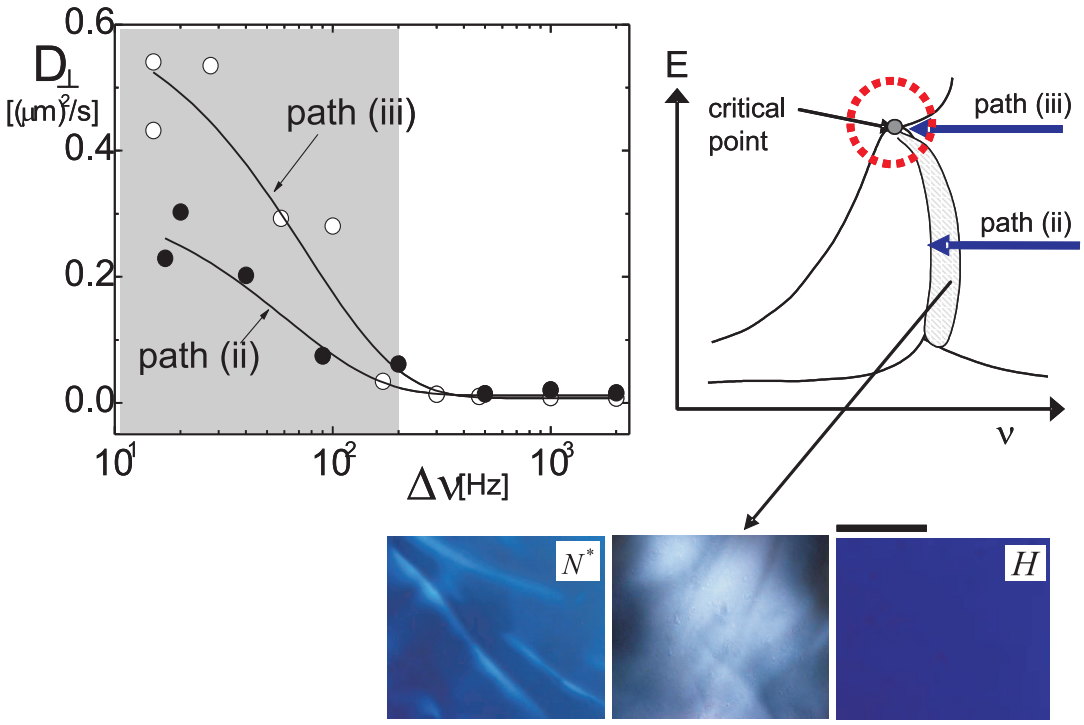

Figure 8: The measured diffusion coefficient $\Gamma_\perp/q^2$ for the pathway (ii) (filled circles) and pathway (iii) (open circles), as a function of the distance $\Delta\nu$ in frequency from the transition line. Various depolarized optical morphologies are shown below. The image in between the images for $N^\star$ and H shows a transient nematic domain that is seen in the shaded region in the top-right sketch of the phase/state diagram. This shaded region corresponds to the shaded area in the plot on the left.

to the H-to-N transition line. For pathway (ii), however, the relaxation rates are strongly increasing on approach of the H-to-$N^\star$ transition line, as can be seen from Fig.7b. More than about 100 to $200\,Hz$ away from the H-to-$N^\star$ transition line, well within the H-phase, the relaxation rates become independent of the frequency and are equal to those measured for pathway (i) (data not shown). The same features are exhibited along pathway (iii). Since the inverse relaxation rates vary linearly with q^2, we can define an effective diffusion coefficient $D_\perp = \Gamma_\perp/q^2$. The diffusion coefficients are plotted in Fig.8 for the off-critical pathway (ii) (filled symbols) and the critical pathway (iii) (open symbols). This shows more clearly the strong increase of relaxation times within a region of $100 - 200\,Hz$ near the H-to-$N^\star$ transition line. The relaxation rates along path (iii), well within the H-phase, are again equal to that for pathways (i) and (ii). The diffusion coefficients for $\Delta\nu > 200\,Hz$ are found to be in the range $(0.013 \pm 0.004)\,(\mu m)^2/s$ both both pathways (ii) and (iii). Hence, the relaxation rates for diffusion perpendicular to the director are independent of frequency and field amplitude within the entire H-phase, except for a small region with a width of about $100 - 200\,Hz$ near the H-to-$N^\star$ transition line. This small region in the phase diagram is indicated in the top-right sketch of the phase/state diagram in Fig.8 by the shaded area, and corresponds to the shaded region in the plot for the diffusion coefficient.

The reason for the faster dynamics in the vicinity of the H-to-$N^\star$ transition line is due to the presence of pre-transitional, transient nematic domains. Such a domain is shown in the depolarized microscopy image in Fig.8, in between the images for the $N^\star$- and H-phase. Near the critical point the size of these domains is much larger than the domains observed along the off-critical pathway. The domains appear and disappear on a time scale of a few minutes. The local nematic director within these domains is not oriented along the electric field. Dynamic light scattering therefore also probes diffusion of rods within the pre-transitional domains in directions parallel to the director. The increase of the measured diffusion coefficient on approach of the transition line is therefore attributed to diffusion parallel to the director within the pre-transitional domains. Since diffusion parallel to the director is faster, the measured diffusion coefficient increases as more of the nematic domains are formed near the transition line. The fact that, within the region where pre-transitional domains

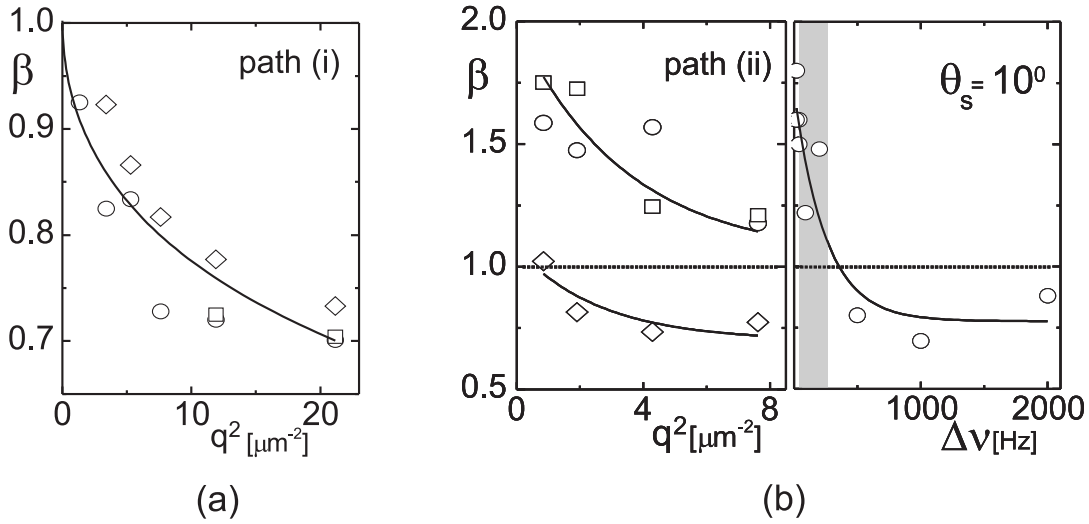

Figure 9: On the left: the stretching coefficient β as a function of q^2 for three distances from the transition line for the off-critical path (ii): $\Delta\nu = 20$ (circles),200 (squares) and $2000\,Hz$ (diamonds). The largest scattering angle here is 20^0. Middle: the stretching coefficient for pathway (ii), for three frequencies with $\Delta\nu = 20\,Hz$ (circles), $200\,Hz$ (squares) and $2000\,Hz$ (diamonds). On the right: the stretching coefficient for a scattering angle of 10^0 as a function of $\Delta\nu$ is shown for path (ii). Solid lines are guides-to-the-eye.

are present, the apparent diffusion coefficient along pathway (iii) is larger as compared to pathway (ii) indicates that there are relatively more rods oriented perpendicular to the field along the critical pathway. That is, domains have a preferential orientation perpendicular to the field near the critical point.

Diffusion can be super-diffusive (in the sense that $\beta > 1$) or sub-diffusive ($\beta < 1$), depending on the scattering wave vector q and the distance from the H-to-$N^\star$ transition line. As can be seen from the left plot in Fig.9, diffusion along pathway (i) is always sub-diffusive. For very small scattering wave vectors, normal diffusion (where $\beta = 1$) is approached. The behavior of β for pathways (ii) and (iii) are very similar, so that we show only data on the former in the two plots on the right in Fig.9. As can be seen, diffusion is sub-diffusive well within the H-phase. The stretching coefficient as a function of q is the same as for pathway (i) to within experimental error. The stretching coefficients thus seem to be the same throughout the H-phase, and only depend on the scattering wave vector. Diffusion is super-diffusive only within the region where pre-transitional domains are present. This is probably related to the strong inhomogeneities that exist in this region of the phase/state diagram. The plot in Fig.9 on the right shows the variation of β at a fixed q (corresponding to a scattering

angle of 10^o) as a function of the distance from the H-to-$N^\star$ transition line. The value of β seems to become equal to 2 for small wave vectors at the transition line. An understanding of the behavior of the stretching exponent requires a microscopic theory for the rod-dynamics within the H-phase, which is not yet existing.

We can conclude that the degree of orientational order and the microscopic dynamics corresponding to displacements perpendicular to the electric field are essentially independent of frequency and field amplitude well within the H-phase, away from the H-to-$N^\star$ transition line. There are significant frequency dependencies, only close to the H-to-$N^\star$ transition line, due to the existence of pre-transitional nematic domains, which have a typical life time of a few minutes. Due to these "anomalous" domains, diffusion can be strongly super-diffusive, especially for small wave vectors. Within the H-phase, perpendicular diffusion is sub-diffusive. Furthermore, on approach of the critical point from the H-phase, a slow decaying relaxation process is observed. The critical features of this point on approach from the dynamical state as described in Ref.[16] is thus also present for approach from the H-phase.

5 Conclusions

A number of phases and dynamical states are induced in a concentrated suspension of charged, colloidal rods (fd-viruses) by an external electric field. We performed electric birefringence and small angle dynamic light scattering experiments along different pathways within one of the phases, the H-phase, which is a homogeneous phase with homeotropic alignment. The H-phase exists for frequencies larger than about a kHz. Since at frequencies higher than a few kHz the diffuse double layers and the layers of condensed ions of the colloidal rods are only weakly polarized, it is not yet clear by which mechanism the H-phase is stabilized. Since electro-osmotic flow is established on a much smaller time scale (of the order of a ns), the field independent response within the H-phase might be due to rod-rod interactions induced by this solvent flow.

The key finding of this paper is that diffusion in the direction perpendicular to the electric field (which is also the direction of orientation of the rods) and the degree of orientational order in the H-

phase is independent of the applied frequency and field amplitude. This suggests that the rod-rod interactions that stabilize the H-phase are not due to charge-polarization, but are due to hydrodynamic interactions through electro-osmotic flow. As yet there is no theory that could explain these observations. Only quite near to the H-to-$N^\star$ transition line (within a frequency interval of about $100 - 200\,Hz$), we found an increase of perpendicular diffusion coefficients. This is due to the existence of pre-transitional nematic domains with a director that is not parallel to the electric field. The life time of these domains is typically a few minutes and are visualized by means of polarization microscopy.

There is a point in the phase/state diagram where several transition lines meet. This point has been shown [16] to exhibit a diverging time- and length-scale on approach from the side of the dynamical state. We have observed an extremely slow mode on approach of this non-equilibrium critical point also from the side of the H-phase. In addition, the size of the pre-transitional domains is much larger than for an off-critical approach of the H-to-$N^\star$ transition. The characterization of the critical behavior within the H-phase needs further study.

Acknowledgments

This work is partially supported by the EU-FP7 Network "Nanodirect" (contract number CP-FP-213948-2).

References

[1] U. Dassanayake, S. Fraden, A. van Blaaderen, J. Chem. Phys. **112**, 3851 (2000).

[2] A. Yethiray, A. van Blaaderen, Nature (London) **421**, 513 (2003).

[3] F. Mantegazza, T. Bellini, M. Buscaglia, V. Degiorgio, D.A. Saville, J. Chem. Phys. **113**, 6984 (2000).

[4] K. Kang, J.K.G. Dhont, Euro. Phys. Lett. **84**, 14005 (2008).

[5] K. Kang, J.K.G. Dhont, Soft Matter **6**, 273 (2010).

[6] W.B. Russel, D.A. Saville, W.R. Schowalter, *"Colloidal Dispersions"* (Cambridge University press, March 1992).

[7] D. Saintillan, E. Darve, E.S.D. Shaqfeh, J. Fluid Mech. **563**, 223 (2006).

[8] G. S. Manning, Eur. Phys. Lett. **86**, 36001 (2009).

[9] G. S. Manning, Eur. Phys. J. E, **30**, 411 (2009).

[10] C. Graf, H. Kramer, M. Deggelmann, M. Hagenbüchle, C. Johner, C. Martin, R. weber, J. Chem. Phys. **98**, 4920 (1993).

[11] Kramer, H., Graf, C., Hagenbuche, M., Johner, C., Martin, C., Schwind, P., Weber, R., J. Phys. II France, Vol 4, 1061 (1994).

[12] J. Newman, H. L. Swinney, L. A. Day, J. Mol. Biol. **116**, 593 (1977).

[13] J. Sambrook, E.F. Fritsch, T. Maniatis, *Molecular Cloning : A Laboratory Manual* (Cold Spring Harbor Laboratory Press, New York, 1989).

[14] K. Kang, A. Wilk, A. Patkowski, J.K.G. Dhont, J. Chem. Phys. **126**, 214501 (2007).

[15] K. Zimmermann, J. Hagedorn, C.C. Heuck, M. Hinrichsen, J. Ludwig, J. Bio. Chem. **261**, 1653 (1986).

[16] K. Kang, J.K.G. Dhont, Eur. Phys. J. E, **30**, 333 (2009).